

Multiphasic liquid flow as a universal tool for nanofabrication of diverse polymer morphologies

Rachel Bang

North Carolina State University <https://orcid.org/0000-0003-0568-5136>

Sangchul Roh

North Carolina State University <https://orcid.org/0000-0003-3268-6214>

Austin Williams

North Carolina State University <https://orcid.org/0000-0003-4080-5164>

Simeon Stoyanov

Wageningen University <https://orcid.org/0000-0002-0610-3110>

Orlin Velev (✉ odvelev@ncsu.edu)

North Carolina State University <https://orcid.org/0000-0003-0473-8056>

Letter

Keywords:

Posted Date: March 14th, 2022

DOI: <https://doi.org/10.21203/rs.3.rs-1341600/v1>

License:   This work is licensed under a Creative Commons Attribution 4.0 International License.

[Read Full License](#)

Abstract

Soft matter of synthetic and biological origin find application in a range of consumer products such as rheological modifiers, structural adhesion enhancers, nonwovens, and membranes¹. The functionality of materials typically derives from their nano- and microscale structure and overall morphology¹⁻³. Many fabrication techniques are capable of producing morphologies including particles⁴, fibers^{4,5}, and membranes^{6,7}. Yet, these techniques may be limited in producing a few specific morphologies and in fine-tuning nano- or microscopic features. Many are also resource and energy-intensive, restricting their potential as commercial processes⁸. Here, we explore interfacial polymer precipitation within sheared multiphasic systems. Through systematic investigation of critical processing parameters, we observe the fabrication of twelve unique polymer morphologies. We verify that the liquid shear-based technique is versatile and works well with chemically diverse polymers, showing potential as a universal tool for fabricating many morphologically distinct polymer structures by simple, scalable processes.

Full Text

The multiphasic shear technique draws inspiration from two fabrication methods: phase inversion via nonsolvent-solvent (NS-S) exchange and interfacial polymerization or precipitation. These methods can produce particles⁹⁻¹⁰, fibers¹⁰⁻¹³, or membranes^{6,7} while allowing the controlled formation of nano- or microscopic features^{6,9,10}. Our previous investigations revealed that such processes can be transcribed to multiphasic fluids and highlighted the role of hydrodynamic shear in developing diverse structures. Initial research revealed the formation of microrods and fibers within laminar flow^{1,14,15}. Within turbulent flows, the shear-based technique led to the discovery of intricate structures such as dendritic soft matter (“dendricolloids”) and sheets¹. Other researchers have since adopted derivative methods for producing polymer microrods^{16,17}, other types of dendricolloids¹⁸, and sheets¹⁹. These studies highlight the technique’s capability for producing polymer structures tailored for specific applications.

We performed the initial experiments using polystyrene (PS) to ensure that the chemical composition does not contribute to structural variability. Initially, a polymer is dissolved in a good solvent. The polymer solution is injected into sheared nonsolvent medium, miscible with the polymer solvent, within two fabrication platforms. Laminar flow conditions were investigated using a Couette flow device (40-6,000 rpm) (Fig. 1a). Turbulent flow was produced through a high-shear colloidal mill, IKA Magic Lab® (3,000-26,000 rpm) (Fig. 1b, full details in the Methods section). The ultralow interfacial tension between the miscible solvent and nonsolvent allows for extreme liquid-liquid surface deformation upon shearing until the polymer is fully precipitated.

The outcome of this seemingly simple procedure is a result of the interplay of multiple underlying processes described briefly here and in more detail in the Supplementary Information. We constructed a simple conceptual framework that distinguishes three operational fabrication “stages”. The first physical mechanism determining the outcome is fluidic shear as the continuous-phase nonsolvent medium’s streamlines “template” themselves onto the dispersed polymer solution phase^{1,14}. The second stage

involves the competition between bulk shear and interfacial stress. It is associated with polymer molecular entanglement which affects the dynamic capillary stability of the polymer solution stream during precipitation²⁰ or the mechanical integrity of the precipitated structure^{14,15}. The final key mechanism is the precipitation rate, relating to the rate of interfacial NS-S exchange based on their mutual affinity or miscibility. It can be described by the interaction parameter, χ_{12} , between the nonsolvent (1) and the solvent (2)^{6,7}.

The types of polymer morphologies resulting from the process were investigated systematically by variations of two fluid regimes (laminar and turbulent), two states of polymer entanglement (low and high), and three precipitation rates (delayed, balanced, and rapid). These sub-stages resulted in twelve unique processing combinations and revealed a rich variety of polymeric structures. Simpler structures such as microparticles, rods, fibers, and ribbons are formed within laminar flows (Fig. 1c–h). Structures ranging from nanoparticles to porous nanosheets are formed within turbulent flows (Fig. 1i –n). We will focus on certain morphologies to investigate the critical control parameters. Other morphologies not discussed here in detail are described in the Supplementary Information.

We first elaborate on the effects of shear rate and polymer solution concentration on PS structures fabricated within a Couette flow device (Fig. 2a). This device produces flows ranging from strictly laminar Couette flow to modulated waves²¹. Several concentrations of PS and tetrahydrofuran (THF) solutions were injected into water. Cloud points were measured to approximate the binodal curve on the ternary diagram (Fig. 2b). The shapes and sizes of precipitated structures were found to depend on the polymer solution density (ρ) and viscosity (μ), interfacial tension (γ), fluid velocity (u), and precipitation rate (represented by χ_{12}) (Fig. 2c). Most of these variables can be collectively described by the Reynolds (Re), Capillary (Ca), and Weber (We) numbers which express the relative importance of inertial, viscous, and cohesive forces. Furthermore, they can describe the fluid characteristics of the nonsolvent medium as well as injected solution stream dripping, jetting, and subsequent droplet breakup due to Rayleigh-Plateau instabilities^{20,22}.

The simplest structures formed in the Couette cell device were microparticles. The formation of particles with low polymer chain entanglement is a “trivial” outcome of nonsolvent-induced precipitation, following supersaturation or nucleation and growth mechanisms²³. Droplets can form through dripping mechanisms or break off after jetting due to capillary fragmentation before polymer precipitation can counteract the liquid-liquid phase breakup (Fig. 2d). Rods can be formed by two alternative pathways (Fig. 2e): additional shearing of polymer droplets formed as described above¹⁷ or through structural fragmentation due to limited mechanical integrity after the polymer has separated as a solid phase¹⁴.

Above a critical entanglement concentration, C_e , evaluated to be 2.5 – 3 wt. % PS in THF (Supplementary Fig. 1), fibers and ribbons are observed. A transition from fibers to ribbons can be observed with increased polymer concentration and shear rates. The concentration not only dictates molecular chain entanglement, but also the onset of phase separation as more concentrated solutions requires a lesser

amount of nonsolvent influx to precipitate. The intensified interfacial mass transport at higher polymer concentrations is analogous to an earlier onset of phase separation, as suggested by the decreasing nonsolvent to solvent ratios (NS:S) (Fig. 2b). The subtle morphological difference between fibers and ribbons may be explained by different collapse modes of a denser “skin” layer due to variances in precipitation rate (Fig. 2a and Supplementary Fig. 2a).

On average, the characteristic dimensions (d_c) of particles (diameter), fibers (diameter), and ribbons (principal axis of cross-section) decreased with increasing nonsolvent flow velocity and decreasing polymer concentration (Fig. 2a and Supplementary Fig. 2b). This was expected as the d_c of the structures generally have an inverse relationship to the continuous-phase Re_c , continuous-phase Ca_c and dispersed-phase We_d (Supplementary Information). To illustrate, when the shear rate increased from 20 to 600 s^{-1} (approximately 60-fold increase in Re_c and Ca_c), the diameters of fibers formed from 5 wt. % PS solution decreased 4-fold. Increasing shear stress by changing the viscosity of the nonsolvent medium was also found to decrease the characteristic size of structures (Supplementary Fig. 3).

The results deviated slightly from what was predicted through Re , Ca , and We analysis. Despite expecting of dripping characteristics at conditions with low Ca_c and We_d^{20} , all particles were formed by droplet breakup after jetting, and even observed the production of fiber and ribbon-like structures in predicted dripping conditions (Supplementary Fig. 4 and Information). We also estimated that a transition from Couette flow to Taylor vortex flow around Re_c of 125. Despite fabrication within strictly non-laminar flows, we still obtained “one-dimensional” fibers and ribbons within these regimes and do not observe branching morphologies until shear rates close to 600 s^{-1} . These outcomes may point to contributions of more complex effects such as the elastocapillarity response of the injection polymer solution^{24,25}.

In turbulent flow conditions, the resulting morphologies change profoundly. The disruptive nature of the turbulent flow leads to rapid droplet fragmentation, forming under low entanglement conditions particles of average size of several hundred nanometers in diameter (Fig. 1i). Slightly higher PS concentrations yielded the formation of “mesorods,” similar in shape to the microrods obtained in laminar flow but approximately one order of magnitude smaller in size (Fig. 1j). Ternary systems with faster precipitation rates and insufficient entanglement produced amorphous chunks (Fig. 1k). The results outlined in Fig. 3a show that above the critical entanglement concentration, we see three distinct classes of structures: dendricolloids (Fig. 1l), branched-ribbons (Fig. 1m), and nano-sheets (Fig. 1n).

Dendricolloids constitute a unique class of soft matter with high degree of branching that we reported earlier¹. These particles are fabricated in turbulent flows which are characterized by multi-scale vortices that transport energy through a cascade until dissipated by viscous means at the Kolmogorov length scale, the smallest vortex scale²⁶. We expected that an increased shear rate would increase the rate of energy dissipation and template finer features on the particles (Supplementary Information). The rheological properties of dendricolloid suspensions exhibited increasing gelation efficiency with increasing dissipation conditions despite lack of relation between lengths of the terminating branches of

dendricolloid particles and the fabrication shear rate (Supplementary Fig. 5a,b). These results, alongside data from rheological experiments using dendricolloids fabricated with different rotor-stator gap dimensions (Supplementary Fig. 5c), indicate that larger shear stresses on the polymer solution droplets lead to the formation of dendricolloids with enhanced branching and gelation capabilities

Dendricolloids could transition into a previously unreported class of dendritic particles with ribbon-like branches, which have increased gelation propensity compared to dendricolloids (Supplementary Fig. 5d). The transition can be controlled by the polymer solution concentration (Fig. 3a) or by choice of the ternary system. PS solutions composed of two solvents, THF and 1,4-dioxane, were injected into sheared water (Fig. 3b,c). The THF ternary system has a lower NS-S affinity than the 1,4-dioxane system with χ_{12} values of 1.56 and 1.13, respectively, for 50 v.% water^{7,27}. Thus, droplets of the THF system can undergo significant interfacial deformation compared to those of the 1,4-dioxane system, which has faster onset of precipitation as suggested by its smaller one-phase region, leading to the formation of thin sheets. The formation of branched ribbons was accomplished by injecting PS/1,4-dioxane solution into 20 v.% 1,4-Dioxane (aq.). These results confirmed that varying the precipitation rate is analogous to varying the polymer concentration and can achieve similar morphological transitions.

Porous nanosheets are structures that we have characterized in detail for the first time (Fig. 1k). We hypothesize that the morphology is a result of the rapid interfacial precipitation of a polymer “skin” which is subsequently peeled off by the vigorous flow. Slight differences in precipitation rate were observed to change the material’s nanoscale thickness and porosity (Fig. 3d). The 1,4-dioxane ternary system has relatively slower precipitation rates than other systems (Fig. 3e) and produced sheets with average thicknesses around 100 nm. In contrast, faster precipitation by the dimethyl formamide (DMF) system produced sheets with 4× larger thicknesses. This supports the theorized mechanism of sheet formation as the faster NS-S exchange will increase the precipitation depth into the solution droplet before the skin is sheared off. Superficially, faster precipitation rates also correlated with an increase in effective pore diameter. However, a closer look at the nanoscopic porous features rather suggest differences in phase separation mechanisms (Fig. 3d). The 1,4-dioxane system sheets have distinct individual pores while the DMF system produced bi-continuous sheets. The different pore characteristics are in line with previous observations of phase inversion mechanisms for membranes^{7,28}.

One of the most surprising findings of this study is the diversity of materials morphologies that can be formed by this operationally simple method. It could be expected that the outcomes of such a complex process will be largely chaotic and difficult to control, especially for the case of turbulent flow. The nature of the fluid flows leads to some degree of size and mass variation in particles made in the same processing conditions. However, we observed that the resulting structures are distinctly different in their nano- or microscopic features, and their bulk properties are well reproducible. The scheme in Fig. 4 summarizes the mechanisms and outcomes leading to liquid-shear fabrication of twelve classes of polymer material morphologies. While this conceptual breakdown does not focus on the smaller intricate processing condition details, it highlights the delineation of the major physical effects involved. The key role of **shear flow** is established by the results which generally support the mechanism of fluid streamline

templating of the precipitating polymer. The **balance of interfacial and shear stresses** heavily influenced the polymeric structures both during and after polymer precipitation. Finally, the **rate of polymer precipitation** was found to be a significant factor as the ratio of precipitation to shearing rates governs the extent to which fluidic characteristics are templated in the resulting morphologies.

The liquid shear-based fabrication technique investigated here combines complex multiphase flows with spontaneous interfacial mass-transport that induces phase separation and precipitation. We demonstrated the universal nature of these principles by transcribing them to the fabrication of three other common polymers of synthetic or biological origin. The polymers were selected for their diverse chemical composition and properties: copolyester, polyvinylidene fluoride (fluorinated polymer used in battery separators), and chitosan (common biopolymer). We found that the same morphologies that were produced with PS shown in Fig. 1 can be fabricated for these other polymers with judicious selection and adjustment of the processing parameters (Supplementary Fig. 6 with corresponding processing conditions listed in Supplementary Fig. 7). It is clear that the physical principles can also be adapted to a broad range of polymers in addition to systems that require different fabrication mechanisms such as cross-linking²⁹. These results support our findings that liquid-liquid fabrication principles can be used to make a broad range of polymeric materials with diverse compositions and target areas of application. For example, microrods can be used as foam stabilizers¹⁵ or in liquid crystal systems¹⁶. Nanofibrillar or nanoporous materials can be used in water cleanup and remediation^{7,8,11}. Other applications include adhesives and coatings¹, homocomposite hydrogels²⁹, and battery separators or electrodes^{18,19,30}. The new structures reported here can find further use in applications ranging from colloidal systems to energy and biomedical materials.

In summary, the examination of the effects of hydrodynamic shear, molecular entanglement, and precipitation rate prove that liquid-liquid precipitation in sheared multiphase fluid could be used in scalable fabrication of multiple classes of polymeric soft matter. It provides precise control over morphological transitions and nano- and micro-scale characteristics such as cross-section, thickness, or pore size. Polymer materials of all diverse morphologies presented here could be produced consistently, precisely, and potentially on unprecedented scale if the method is implemented in continuous flow devices. Most importantly, we believe that insights into the fundamental mechanisms underlying this shear-based process could help establish an intellectual framework guiding the development of future liquid-liquid nanomanufacturing technologies.

Materials And Methods

1.1 Materials

Most morphologies were fabricated from polystyrene (weight-averaged molecular weight $M_w \sim 5,798, 192,000, \text{ and } 230,000$, Sigma-Aldrich). Polystyrene was dissolved in the following solvents: tetrahydrofuran (VWR), chloroform (99% anhydrous, Sigma-Aldrich), N,N-dimethylformamide (Fisher Scientific), N,N-dimethylacetamide (Sigma-Aldrich), 1,4-dioxane (99.8% anhydrous, Sigma-Aldrich), and

ethyl acetate (99.5%, Acros Organics). Nonsolvents used were deionized water and ethanol (anhydrous, VWR).

Additional polymers used were poly(vinylidene fluoride) (average $M_w \sim 530,000$, Sigma Aldrich), polyester (Ecdel PCCE 9966 copolyester ether elastomer, Eastman), and chitosan (77% deacetylated, Sigma Aldrich). Solvents for these were dimethylsulfoxide (anhydrous, $\geq 99.9\%$, Sigma Aldrich), chloroform (anhydrous, $\geq 99.9\%$, contains 0.5-1.0% ethanol as stabilizer, Sigma Aldrich), and 1.5% acetic acid (hygroscopic, Acros Organics). The nonsolvents were ethanol and methanol (Chromasolv® for HPLC, $\geq 99.9\%$, Sigma Aldrich).

1.2 Fabrication platforms and production

In order to sample the entire range of fluidic regimes, two fabrication platforms are used which are also described in detail in Roh et al.¹ Laminar to weakly turbulent flow is modeled using a simple Couette cell, which is also capable of developing turbulent Taylor vortices at higher rotational speeds. This type of apparatus was chosen since Taylor-Couette flow is well-studied and the parameters are easily controlled. An acrylic baffle was placed at the top of the fluid to reduce boundary effects. The baffle also maintained the same injection position within the apparatus. Polymer solution was injected in the middle of the shearing gap, and calculated shear rates and Re are based on the shear rate in the middle of the gap.

An IKA Magic Lab device (IKA Works Inc., Wilmington, NC, USA) with MK module is used for producing extremely turbulent flows (3,000 – 26,000 rpm). The module has a conical rotor with a stator which axially displaces to adjust the shearing gap from 80 – 650 μm . This device should produce turbulent flows at all operational speeds. Due to serrations on the rotor-stator, it is difficult to precisely estimate the true shear rates and flow characteristics due to a probability of cavitation at the higher shear rates. Our approximation of shear rates, not considering the complex rotor-stator geometry, gives a shear rate range of 39,000 – 157,000 s^{-1} .

Unless otherwise specified, morphologies were fabricated with a Couette cell with $n = 0.65$ and IKA Magic Lab with 250 μm shearing gap and 20,000 rpm. Polymer solutions used in this study ranged from 0.1 – 20 wt.% in various solvents and primarily were made with PS of 230 kDa molecular weight. The solutions were injected into the nonsolvent shearing medium at approximate rates of 0.05 mL/min and 2.5 mL/min for the laminar and turbulent platforms, respectively. In each fabrication run, the volume of polymer solution injected was maintained below 10 v.% of the amount of nonsolvent medium. After complete fabrication, the particles were collected and washed several times in ethanol before storage.

1.3 Building ternary phase diagrams

Binodal curves were found through cloud point tests. Various concentrations of polymer solution as components of different ternary systems, were titrated with nonsolvent medium with stirring until the solution became opaque and would separate into two phases upon rest. All diagrams were obtained with PS of 230 kDa, except for the binodal curve for nonsolvent system of 20% Dioxane (aq) which was found

using PS with molecular weight of 190kDa. The NS:S ratios at the onset of phase separation were calculated based on the amount of nonsolvent added at the point of opacity.

1.4 Imaging

The morphologies were visualized mainly by a bright field and fluorescence microscope (BX-61 Olympus) and field emission scanning electron microscope (FEI Verios 460L). Material preparation for imaging includes dilution in ethanol and sonication (~ 10 min) prior to spin-coating (2000 rpm) onto the imaging substrate, glass slide or silicon wafer, to limit particle entanglement and aggregation. Phase contrast filters were used with bright field microscopy. Samples for SEM imaging were coated with Au-Pd nanoparticles (approximately 5 nm layer) for sufficient electron conduction. Only the chitosan particles in Fig. 5 were not coated.

Image analysis was performed with ImageJ software with SEM images for approximating characteristic dimensions of the morphologies. The measurements for the particles, fibers, and ribbons from Fig. 2a and Supplementary Fig. 2a were conducted manually and the sample sizes (N) for 1, 2.5, 5, 10, and 15 wt.% were all between 17 and 2014. The effective pore diameter measurements for Fig. 3 were done by measuring the average area of the pores then calculating the associated diameter if the pores were circular. Sample size of pore size measurements ranged from 3390 to 9995 while those for thickness measurements ranged from 3 to 9. Terminating branch lengths in Fig. S5a were measured manually and the sample sizes for the fabricated PS SDCs in 5,000, 10,000, 15,000, and 20,000 rpm conditions were $22 < N < 39$ for 2.5 wt.% PS/THF and $50 < N < 133$ for 5.0 wt.%.

1.5 Viscosity and rheological characterization

The viscosities of polymer solutions, ranging from 0.1 to 7.4 v.%, were measured using a Ubbelohde viscometer (calibration constant = $0.09738 \text{ (mm}^2 \text{ s}^{-1} \text{ s}^{-1})$). Sample of PS in THF with concentrations ranging from 0 to 7.4 v.% were prepared. Viscometer was carefully filled with appr. 25 mL of polymer solution. Solution was pulled through the tubes with a macro pipette prior to measurement.

The viscoelastic properties were used to approximate the degree of gelation in particle suspensions. The material, already suspended in ethanol after washing procedures, were resuspended in pure polyethylene glycol 400 (Acros Organics, average M.W. 400, $d = 1.1275$) to have final weight concentrations of 0.5-1.5 wt. %. PEG 400 was chosen as the suspension medium to show greater gelation propensity using PS SDC particles compared to cellulose acetate (CA) SDCs (CA SDCs were used in Roh et al. at similar particle concentrations and showed more fluid-like behavior due to refractive index matching). We did not see a need to reduce van der Waals forces so the suspension medium did not have matching refractive index with PS. The SDC-EtOH-PEG 400 mixtures were gently mixed at room temperature until all ethanol had evaporated. The samples were evaluated at 25°C using a rheometer (Discovery HR-2, TA instruments) equipped with a sand-blasted plate (40 mm diameter) and gap size of 800 μm . Frequency sweeps were performed at 1% strain for $100 - 0.1 \text{ rad s}^{-1}$, and amplitude sweeps were performed at 1 rad s^{-1} from 0.01 - 1000% strain.

Declarations

Online content

Any methods, additional references, Nature Research reporting summaries, source data, extended data, supplementary information, acknowledgements, peer review information; details of author contributions and competing interests; and statements of data and code availability are available in the online version of the paper.

Data and materials availability

All data supporting the findings in this study are available in the manuscript and the supplementary materials.

Acknowledgements

This study was supported by grants from US National Science Foundation, CMMI-1825476 and partially EFMA-2029327. The visualization studies were performed in part at the Analytical Instrumentation Facility (AIF) at North Carolina State University, which is supported by the State of North Carolina and the National Science Foundation (award number ECCS-2025064). The AIF is a member of the North Carolina Research Triangle Nanotechnology Network (RTNN), a site in the National Nanotechnology Coordinated Infrastructure (NNCI). The authors acknowledge Dr. Lilian Hsiao for the use of her lab rheometer.

Author contributions

The initial conceptualization of this research was provided by ODV, SR and SS. The methodology was put in place by RSB, SR, SS and ODV. The experimental research investigation was performed by RSB, SR and AHW. The figures and visualizations were done by RSB. The funding from this project was obtained by ODV, who also provided supervision and administration. RSB and ODV wrote the paper with feedback and assistance from all co-authors.

Author information and competing interests

NC State University has issued or pending patents on the shear fabrication of nanofibers, dendricolloids and their application in electrochemical energy sources.

References

1. Roh, S., Williams, A. H., Bang, R. S., Stoyanov, S. D. & Velev, O. D. Soft dendritic microparticles with unusual adhesion and structuring properties. *Nat. Mater.* **18**, 1315–1320 (2019).
2. Stamm, M. Nanostructured and nano-size polymer materials: How to generate them and do we need them? in *Nano-Size Polymers: Preparation, Properties, Applications* 3–15 (Springer International Publishing, 2016).

3. Cheng, K. C. K. et al. Templated nanofiber synthesis via chemical vapor polymerization into liquid crystalline films. *Science* (80). **362**, 804–808 (2018).
4. Eda, G. & Shivkumar, S. Bead-to-fiber transition in electrospun polystyrene. *J. Appl. Polym. Sci.* **106**, 475–487 (2007).
5. Koombhongse, S., Liu, W. & Reneker, D. H. Flat polymer ribbons and other shapes by electrospinning. *J. Polym. Sci. Part B Polym. Phys.* **39**, 2598–2606 (2001).
6. Guillen, G. R., Pan, Y., Li, M. & Hoek, E. M. V. Preparation and characterization of membranes formed by nonsolvent induced phase separation: A review. *Ind. Eng. Chem. Res.* **50**, 3798–3817 (2011).
7. Mulder, M. *Basic principles of membrane technology*. (Springer-Science + Business Media, B.V., 1991).
8. Luo, C. J., Stoyanov, S. D., Stride, E., Pelan, E. & Edirisinghe, M. Electrospinning versus fibre production methods: From specifics to technological convergence. *Chem. Soc. Rev.* **41**, 4708–4735 (2012).
9. Udoh, C. E., Garbin, V. & Cabral, J. T. Microporous Polymer Particles via Phase Inversion in Microfluidics: Impact of Nonsolvent Quality. *Langmuir* **32**, 8131–8140 (2016).
10. Haase, M., Stebe, K. & Lee, D. Continuous fabrication of hierarchical and asymmetric bijel microparticles, fibers, and membranes by solvent transfer-induced phase separation (STRIPS). *Adv. Mater.* **27**, 7065–7071 (2015).
11. Qin, J. J., Gu, J. & Chung, T. S. Effect of wet and dry-jet wet spinning on the shear-induced orientation during the formation of ultrafiltration hollow fiber membranes. *J. Memb. Sci.* **182**, 57–75 (2001).
12. Miyazawa, K. Synthesis of fullerene nanowhiskers using the liquid-liquid interfacial precipitation method and their mechanical, electrical and superconducting properties. *Sci. Technol. Adv. Mater.* **16**, 013502–013512 (2015).
13. Zhang, F., Fan, J. & Wang, S. Interfacial Polymerization: From Chemistry to Functional Materials. *Angew. Chemie - Int. Ed.* **59**, 21840–21856 (2020).
14. Smoukov, S. K. et al. Scalable liquid shear-driven fabrication of polymer nanofibers. *Adv. Mater.* **27**, 2642–2647 (2015).
15. Alargova, R. G., Warhadpande, D. S., Paunov, V. N. & Velev, O. D. Foam superstabilization by polymer microrods. *Langmuir* **20**, 10371–10374 (2004).
16. Fernández-Rico, C., Yanagishima, T., Curran, A., Aarts, D. G. A. L. & Dullens, R. P. A. Synthesis of Colloidal SU-8 Polymer Rods Using Sonication. *Adv. Mater.* **31**, 1807514 (2019).
17. Yang, Z. et al. Shear-Assisted Fabrication of Block Copolymer Agglomerates with Various Morphologies in Viscous Medium. *Langmuir* **33**, 2829–2836 (2017).
18. Zhou, H., Zhang, Z., Sun, C., Deng, H. & Fu, Q. Biomimetic Approach to Facilitate the High Filler Content in Free-Standing and Flexible Thermoelectric Polymer Composite Films Based on PVDF and Ag₂Se Nanowires. *ACS Appl. Mater. Interfaces* **12**, 51506–51516 (2020).

19. Cao, X., Zhang, M., Yang, Y., Deng, H. & Fu, Q. Thermoelectric PEDOT:PSS Sheet/SWCNTs composites films with layered structure. *Compos. Commun.* **27**, 100869 (2021).
20. Utada, A. S., Fernandez-Nieves, A., Stone, H. A. & Weitz, D. A. Dripping to jetting transitions in coflowing liquid streams. *Phys. Rev. Lett.* **99**, 094502 (2007).
21. Grossmann, S., Lohse, D. & Sun, C. High-Reynolds Number Taylor-Couette Turbulence. *Annu. Rev. Fluid Mech.* **48**, 53–76 (2015).
22. Groeneweg, F., van Dieren, F. & Agterof, W. G. M. Droplet break-up in a stirred water-in-oil emulsion in the presence of emulsifiers. *Colloids Surf. A: Physicochem. Eng. Asp.* **91**, 207–214 (1994).
23. Conner, C. G., Veleva, A. N., Paunov, V. N., Stoyanov, S. D. & Velev, O. D. Scalable Formation of Concentrated Monodisperse Lignin Nanoparticles by Recirculation-Enhanced Flash Nanoprecipitation. *Part. Part. Syst. Charact.* **37**, 2000122 (2020).
24. Dinic, J. & Sharma, V. Macromolecular relaxation, strain, and extensibility determine elastocapillary thinning and extensional viscosity of polymer solutions. *Proc. Natl. Acad. Sci.* **116**, 8766–8774 (2019).
25. Kibbelaar, H. V. M. et al. Capillary thinning of elastic and viscoelastic threads: From elastocapillarity to phase separation. *Phys. Rev. Fluids* **5**, 092001(R) (2020).
26. McKeown, R., Ostilla-Mónico, R., Pumir, A., Brenner, M. P. & Rubinstein, S. M. Turbulence generation through an iterative cascade of the elliptical instability. *Sci. Adv.* **6**, eaaz2717 (2020).
27. Altena, F. W. & Smolders, C. A. Calculation of Liq-Liq phase separation in a ternary system of a polymer in a mixture of a solvent and a nonsolvent. *Macromolecules* **15**, 1558 (1982).
28. Su, S. L., Wang, D. M. & Lai, J. Y. Critical residence time in metastable region – a time scale determining the demixing mechanism of nonsolvent induced phase separation. *J. Memb. Sci.* **529**, 35–46 (2017).
29. Williams, A. H. et al. Printable homocomposite hydrogels with synergistically reinforced molecular-colloidal networks. *Nat. Commun.* **12**, (2021).
30. Luiso, S. et al. Poly(Vinylidene Difluoride) Soft Dendritic Colloids as Li-Ion Battery Separators. *J. Electrochem. Soc.* **168**, 020517 (2021).

Extended references

31. McKee, M. G., Wilkes, G. L., Colby, R. H. & Long, T. E. Correlations of Solution Rheology with Electrospun Fiber Formation of Linear and Branched Polyesters. *Macromolecules* **37**, 1760–1767 (2004).]
32. Shenoy, S. L., Bates, W. D., Frisch, H. L. & Wnek, G. E. Role of chain entanglements on fiber formation during electrospinning of polymer solutions: Good solvent, non-specific polymer-polymer interaction limit. *Polym. J.* **46**, 3372–3384 (2005).
33. Megelski, S., Stephens, J. S., Bruce Chase, D. & Rabolt, J. F. Micro- and nanostructured surface morphology on electrospun polymer fibers. *Macromolecules* **35**, 8456–8466 (2002).

34. Kulicke, W. M. & Kniewske, R. The shear viscosity dependence on concentration, molecular weight, and shear rate of polystyrene solutions. *Polym. Bull.* **14**, 157–164 (1985).

35. Vankova, N. et al. Emulsification in turbulent flow 1. Mean and maximum drop diameters in inertial and viscous regimes. *J. Colloid Interface Sci.* **312**, 363–380 (2007).

Figures

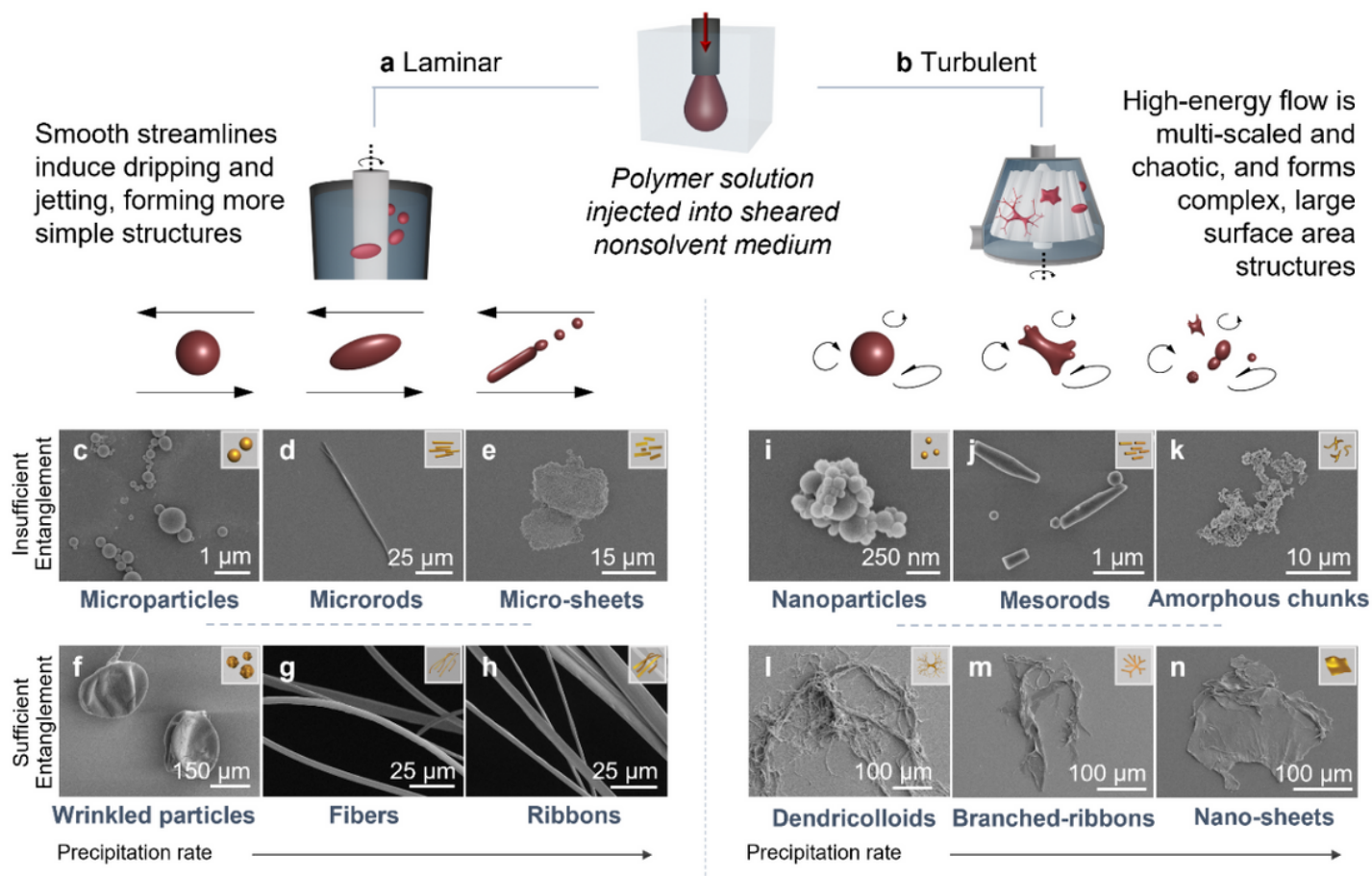


Figure 1

Fabrication routes and morphologies produced with polystyrene (M_w 5.78 and 230 kDa). **a**, The Couette cell platform can produce laminar to weakly turbulent flows. **b**, Turbulent flows are produced within a colloidal mill with a serrated rotor-stator module. These produce fluctuations in pressure and velocity with cavitation. **c - e**, Smooth microparticle and microrod morphologies are formed with low polymer concentration or molecular weights at delayed or balanced precipitation. Micro-sheets are formed during rapid precipitation. **f - h**, Increasing the molecular entanglement will form wrinkled microparticles, ribbons, and fibers. **i - k**, Morphologies created within turbulent flow with insufficient entanglement are smooth nanoparticles, mesorods, and amorphous chunks. **l - n**, Complex hierarchical and porous morphologies

such as dendricolloids, branched-ribbons, and nano-sheets are formed with higher polymer chain entanglement.

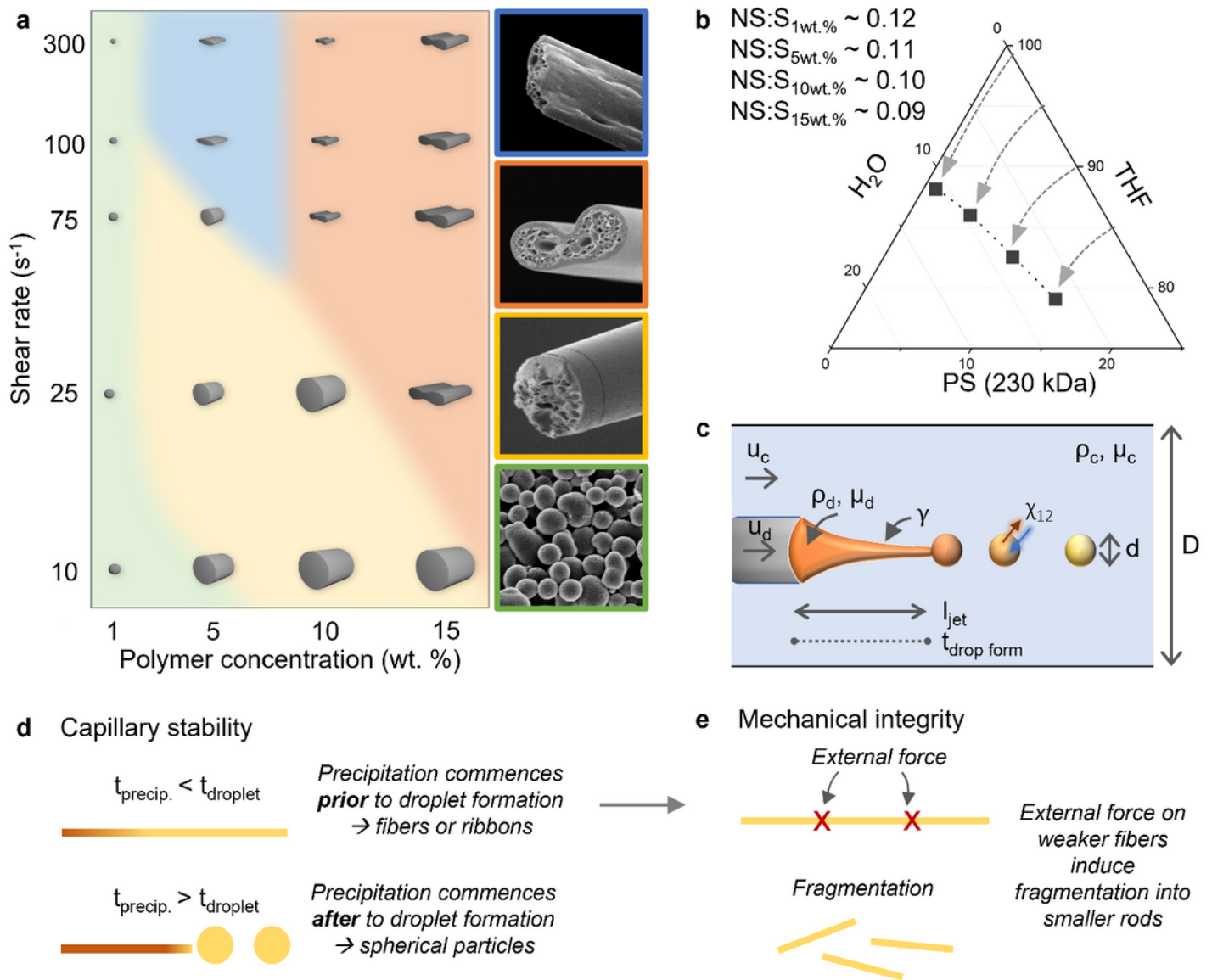


Figure 2

Effects of process parameters on nano- and microscale structures formed within laminar and weakly turbulent flow. **a**, Operational phase diagram outlining the effects of polymer concentration and shear rate on morphology formation. Bubble icons indicate the type of morphology and their relative size. SEM images of each morphology are shown on the right with border colors corresponding to the colors on the diagram. Note, two sub-classes of ribbon morphology are differentiated by cross-section (blue vs. orange). **b**, Approximate binodal curve of PS/THF/H₂O system on equilibrium ternary phase diagram. Nonsolvent-solvent (NS:S) ratios at the onset of phase separation decrease with increasing polymer concentration. Arrows follow general composition path. **c**, System parameters of polymer stream within

Couette cell. The time until a droplet forms from a jet stream of length l_{jet} is $t_{drop\ form}$. The geometric dimension of device, D , is the dimension of the annulus and d is the droplet dimension. Drawing is adapted from figure in Utada et al.²⁰ **d**, Capillary stability describes the balance between viscous and cohesive forces and can determine whether the solution precipitates as droplets or fibers after the onset of jetting. If the ternary system provides rapid precipitation, fibers or ribbons are produced. If the precipitation rate is slow or delayed, the resulting structure is spherical particles. **e**, If the polymer precipitates as longer aspect ratio fibers, but is not able to maintain their morphology due to structural weaknesses, it will fragment into smaller structures.

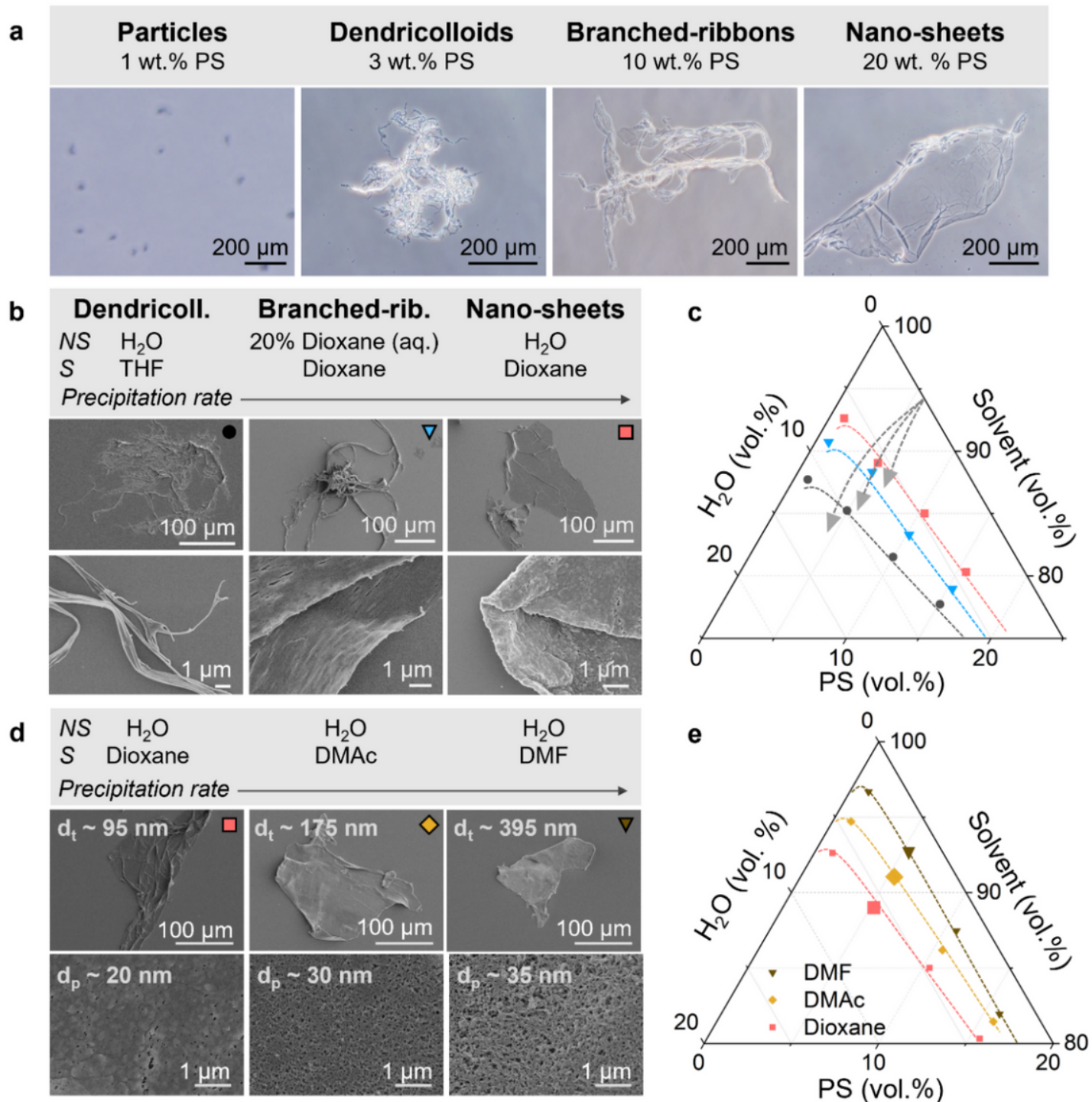


Figure 3

Morphological transitions driven by polymer concentration and precipitation rate in turbulent flows. **a**, Polymer concentrations below the entanglement concentration produced simple particles and rods. Above C_e , more complex dendritic particles and branched ribbon structures are formed. Non-dendritic porous sheets are observed above 15 wt.%. **b**, Similar morphologies fabricated from 5 wt. % PS solution are seen here, although NS-S exchange rates drove the transition between the morphologies. **c**, Ternary phase diagram with approximate binodal curves for PS/THF/H₂O and PS/1,4-Dioxane/H₂O systems. Binodal curve for branched ribbon system (upside down blue triangle) was measured using 192 kDa PS compared to 230 kDa, although we believe the curve should be similar. Arrows show general composition paths. **d**, Nanoscale differences in thickness and effective pore diameters within nano-sheet morphologies due to precipitation rate. **e**, Ternary diagram with binodal curves for ternary systems shown in (d). The affinity between the solvents and water is larger for DMF systems, correlating to a smaller one-phase region.

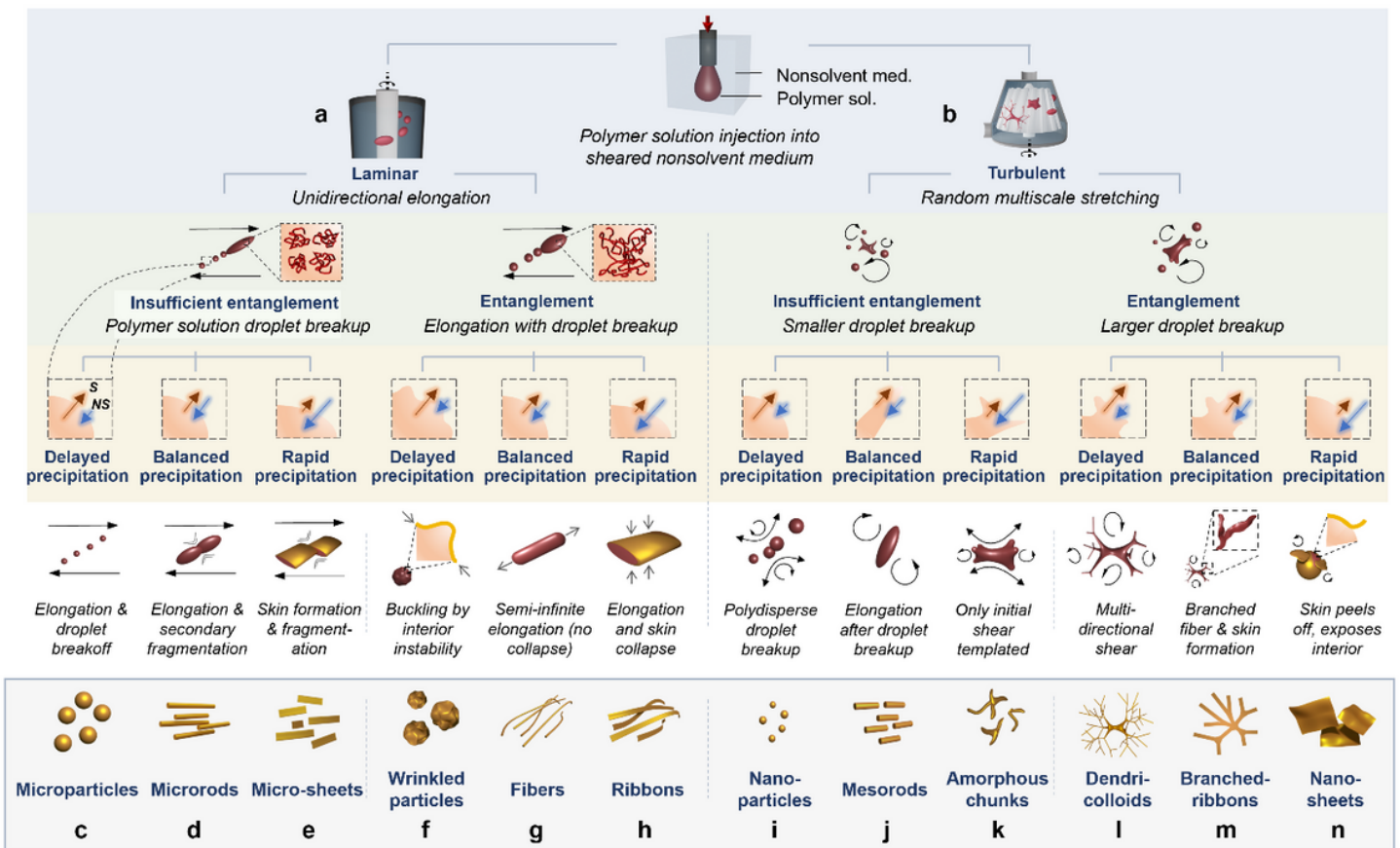


Figure 4

Multi-level schematic of processing conditions of the liquid shear-driven fabrication technique and its resulting morphologies. This technique involves three stages: hydrodynamic shear, capillary stability and mechanical integrity, and precipitation rates. Fluidic shear can be driven by **a**, laminar, or **b**, turbulent flow.

The degree of molecular chain entanglement will determine the formation of polymer solution droplets, their elongation, and the stiffness/strength of the precipitated polymer. The precipitation rate will affect the extent of shearing by decreasing or increasing the ratio of precipitation to shear time scales. The different combinations of these processing conditions enable the formation of a total of twelve polymer structures **c – n**, that are formed by different combinations of process parameters from the three main stages. The mechanisms of formation of the morphologies are shown towards the bottom.

Supplementary Files

This is a list of supplementary files associated with this preprint. Click to download.

- [SupplementaryInformationLiquidnanomanufacturingVelev.pdf](#)